The 4.5 μm full-orbit phase curve of the hot Jupiter HD 209458B

Citation

Published Version

Permanent link

Terms of Use

Share Your Story

THE 4.5 μm FULL-ORBIT PHASE CURVE OF THE HOT JUPITER HD 209458b

ROBERT T. ZELLEM[1], NIKOLE K. LEWIS[2,11], HEATHER A. KNUTSON[3], CAITLIN A. GRIFFITH[1], ADAM P. SHOWMAN[1],
JONATHAN J. FORTNEY[4], NICOLAS B. COWAN[5], ERIC AGOL[6], ADAM BURROWS[7], DAVID CHARBONNEAU[8], DRAKE DEMING[9],
GREGORY LAUGHLIN[4], AND JONATHAN LANGTON[10]

[1] Lunar and Planetary Laboratory, University of Arizona, 1629 East University Boulevard, Tucson, AZ 85721, USA; rzellem@lpl.arizona.edu
[2] Department of Earth, Atmospheric and Planetary Sciences, Massachusetts Institute of Technology, 77 Massachusetts Avenue, Cambridge, MA 02139, USA
[3] Division of Geological and Planetary Sciences, MC 170-25 1200 East California Boulevard, Pasadena, CA 91125, USA
[4] Department of Astronomy and Astrophysics, University of California, Santa Cruz, 1156 High Street, Santa Cruz, CA 95064, USA
[5] Department of Earth and Planetary Sciences, Northwestern University, Technological Institute, 2145 Sheridan Road, Evanston, IL 60208, USA
[6] Astronomy Department, University of Washington, Physics-Astronomy Building, 3910 15th Avenue NE, Seattle, WA 98195, USA
[7] Department of Astrophysical Sciences, Princeton University, 4 Ivy Lane, Peyton Hall, Princeton University, Princeton, NJ 08544, USA
[8] Harvard-Smithsonian Center for Astrophysics, 60 Garden Street MS-16, Cambridge, MA 02138, USA
[9] Department of Astronomy, University of Maryland, College Park, MD 20742, USA
[10] Physics Department, Principia College, 1 Maybeck Place, Elsah, IL 62028, USA

ABSTRACT

The hot Jupiter HD 209458b is particularly amenable to detailed study as it is among the brightest transiting exoplanet systems currently known (V-mag $= 7.65$; K-mag $= 6.308$) and has a large planet-to-star contrast ratio. HD 209458b is predicted to be in synchronous rotation about its host star with a hot spot that is shifted eastward of the substellar point by superrotating equatorial winds. Here we present the first full-orbit observations of HD 209458b, in which its 4.5 μm emission was recorded with *Spitzer*/IRAC. Our study revises the previous 4.5 μm measurement of HD 209458b's secondary eclipse emission downward by ∼35% to $0.1391\%^{+0.0072\%}_{-0.0069\%}$, changing our interpretation of the properties of its dayside atmosphere. We find that the hot spot on the planet's dayside is shifted eastward of the substellar point by $40°9 \pm 6°0$, in agreement with circulation models predicting equatorial superrotation. HD 209458b's dayside ($T_{\mathrm{bright}} = 1499 \pm 15$ K) and nightside ($T_{\mathrm{bright}} = 972 \pm 44$ K) emission indicate a day-to-night brightness temperature contrast smaller than that observed for more highly irradiated exoplanets, suggesting that the day-to-night temperature contrast may be partially a function of the incident stellar radiation. The observed phase curve shape deviates modestly from global circulation model predictions potentially due to disequilibrium chemistry or deficiencies in the current hot CH_4 line lists used in these models. Observations of the phase curve at additional wavelengths are needed in order to determine the possible presence and spatial extent of a dayside temperature inversion, as well as to improve our overall understanding of this planet's atmospheric circulation.

Key words: atmospheric effects – methods: numerical – planets and satellites: general –
planets and satellites: individual (HD 209458b) – techniques: photometric

Online-only material: color figures, machine-readable table

1. INTRODUCTION

Of the more than 1100 transiting exoplanets discovered to date, over 150 are gas giant planets known as "hot Jupiters" that have near-Jupiter masses ($0.5\ M_{\mathrm{Jupiter}} \leqslant M \leqslant 5\ M_{\mathrm{Jupiter}}$) and that orbit very close to their host stars (semi-major axis $a \leqslant 0.1$ AU). These transiting exoplanets are predicted to be tidally locked (e.g., MacDonald 1964; Peale 1974) so that one hemisphere always points toward its host star while the other is in perpetual night. The resulting day-to-night temperature contrast is predicted to drive fast ∼1 km s^{-1} winds, which transfer heat from the dayside to the nightside hemisphere thereby shifting the substellar hotspot and decreasing the day-to-night temperature contrast (e.g., Showman & Guillot 2002; Cooper & Showman 2005, 2006; Showman 2008; Showman et al. 2008b, 2009; Langton & Laughlin 2007, 2008; Dobbs-Dixon & Lin 2008).

One of the best methods to directly constrain the nature of the atmospheric circulation patterns on these planets is to continuously monitor their infrared (IR) emission to characterize the full-orbit phase curve. Such observations yield longitudinal disk variations, which can then be transformed into a longitudinal temperature profile (Cowan & Agol 2008) to measure the redistribution of heat. The *Spitzer Space Telescope* is the only platform currently capable of making mid- to far-IR full-orbit observations due to its stability, continuous viewing capability, and access to longer wavelengths than the *Hubble Space Telescope* (Harrington et al. 2006; Cowan et al. 2007, 2012; Knutson et al. 2007, 2012; Lewis et al. 2013; Maxted et al. 2013).

In this paper, we present new phase curve observations of the hot Jupiter HD 209458b, which has a particularly favorable planet–star radius ratio ($R_p/R_s = 0.12086 \pm 0.00010$; Torres et al. 2008) and orbits a bright star (V-mag $= 7.65$; K-mag $= 6.308$). HD 209458 is a relatively quiet G-type star (e.g., Charbonneau et al. 2000; Knutson et al. 2010), which has been shown to vary by less than ∼0.002 mag at visible wavelengths over a period of 58 days (Rowe et al. 2008). This stability aids in the interpretation of its measured phase curve, as the star can be assumed to remain constant at the level of our measurements. Radial velocity and secondary eclipse observations indicate that this planet has a circular orbit (Henry et al. 2000; Mazeh et al. 2000; Deming et al. 2005; Laughlin et al. 2005; Winn et al. 2005; Wittenmyer et al. 2005; Kipping 2008; Southworth 2008; Torres et al. 2008; Crossfield et al. 2012), and is therefore likely to be in a synchronous rotation state.

---

[11] Sagan Fellow.

HD 209458b's IR dayside emission has been measured during secondary eclipse, when the planet passes behind its host star, with two IRTF/SpeX *K*- and *L*-band eclipses (Richardson et al. 2003), one *Spitzer*/MIPS 24 μm eclipse (Deming et al. 2005), two *Spitzer*/IRS 7–13.2 μm eclipses (Richardson et al. 2007), two *Spitzer*/IRS 7.46–15.25 μm eclipses (Swain et al. 2008), one eclipse simultaneously observed at the four *Spitzer*/IRAC passbands (Knutson et al. 2008), one *Hubble*/NICMOS 1.5–2.5 μm eclipse (Swain et al. 2009), and three *Spitzer*/MIPS eclipses (Crossfield et al. 2012). Multiple studies have used these emission data to constrain HD 209458b's dayside composition and thermal profile (e.g., Burrows et al. 2007; Fortney et al. 2008; Madhusudhan & Seager 2009; Line et al. 2014). The current consensus is that this planet's dayside emission spectrum is best-matched by models with a temperature inversion, possibly from TiO and VO absorption, two molecules typical of cooler stellar atmospheres (Burrows et al. 2007; Knutson et al. 2008; Fortney et al. 2008). However, TiO and VO have yet to be conclusively detected (Désert et al. 2008). Some groups have also argued that TiO would likely be lost to cold traps in the planet's interior and on the nightside (Showman et al. 2009; Spiegel et al. 2009; Parmentier et al. 2013).

Phase-curve measurements indicate a planet's longitudinal brightness temperature variations, allowing for the measurement of heat redistribution from the dayside to nightside. HD 209458b, with an equivalent temperature of 1450 K (assuming a zero albedo) is comparatively cooler than most of the other hot Jupiters for which temperature contrasts have been measured: HAT-P-2b (Lewis et al. 2013), HD 149026b (Knutson et al. 2009a), HAT-P-7b (Borucki et al. 2009), WASP-18b (Maxted et al. 2013), and WASP-12b (Cowan et al. 2012) (see Figure 1 in Perez-Becker & Showman 2013). Thus measurements of HD 209458b's day-to-night temperature contrast enable further exploration of the theory that this contrast is driven by insolation (Perez-Becker & Showman 2013). In addition, the phase curve determines whether HD 209458b, like other hot Jupiters (e.g., HD 189733b; Knutson et al. 2007, 2009b, 2012), has a hot spot shifted eastward of the substellar point. Such a shift would indicate equatorial superrotation, as first predicted by the global circulation model (GCM) of Showman & Guillot (2002).

Here we analyze post-cryogenic *Spitzer Space Telescope* (Werner et al. 2004) IRAC2 (Fazio et al. 2004) full-orbit IR observations of HD 209458b. Our observations probe HD 209458b's dynamical processes by measuring its 4.5 μm dayside emission, location of its hot spot, and day-to-night temperature contrast. Previous secondary eclipse data were obtained in a non-standard observing mode in which *Spitzer* cycled continuously between the four IRAC subarrays (Knutson et al. 2008). This mode enabled coverage of all four bands during a single eclipse event but with one-fifth the effective cadence of the now standard staring mode observations (e.g., Knutson et al. 2012; Lewis et al. 2013). Here we observe continuously in one IRAC band alone, resulting in a higher cadence. We therefore expect that our new observations will allow for a more precise estimate of the 4.5 μm eclipse depth. Our full-orbit data also samples HD 209458b's phase curve and measures for the first time its nightside emission. A previous 24 μm full-orbit phase curve was corrupted by instrumental sensitivity variations (Crossfield et al. 2012). From these data, we compare the hot spot offset, day–night flux differences, and secondary eclipse emissions derived here for HD 209458b with GCMs that predict these values.

2. OBSERVATIONS

The observations were taken between 2010 January 17 20:55:24.4 UT and 2010 January 21 21:28:42.0 UT, resulting in 96.55 hr of data. They begin shortly before secondary eclipse, continue through primary transit, and end shortly after secondary eclipse. To minimize readout time and thereby maximize image cadence, the subarray mode was used in which 32×32 pixel images were stored as sets of 64 in a single FITS datacube with a single image header. By assuming uniform spacing in time, the mid-exposure time for each image is calculated from the header keywords MBJD_OBS (start of the first image in each cube), AINTBEG (integration begin), and ATIMEEND (integration end). Effectively, the image spacing is 0.4 s. We report our timing measurements using BJD_UTC.

2.1. IRAC2 4.5 μm Photometry

The sky background is estimated in each image by first masking out the target star with a 10 pixel radius. 3σ outliers are then trimmed over three iterations to remove hot pixels and cosmic ray hits from the set of 64 measurements at that pixel position from a given data cube. The filtered background counts are fit with a Gaussian function. This count is then subtracted from each image.

We determine the *x*- and *y*-position of HD 209458 in each image using a flux-weighting methodology similar to a centroid that employs a five-pixel-radius circular aperture (e.g., Knutson et al. 2008). We find the latter method results in a more stable position estimate than the center of a two-dimensional Gaussian fit, and a correspondingly smaller scatter in our final photometry, in good agreement with our previous results for *Spitzer* 4.5 μm phase curve observations of HD 189733b (Knutson et al. 2012) and HAT-P-2 (Lewis et al. 2013). We first calculate our photometry using a fixed circular aperture with radii equal to 2.0, 2.1, 2.2, 2.3, 2.4, 2.5, 2.6, 2.7, 2.8, 2.9, 3.0, 3.5, 4.0, 4.5, and 5.0 pixels.

We also explore apertures that scale according to the noise pixel parameter $\tilde{\beta}$, which is defined in Section 2.2.2 (IRAC Image Quality) of the IRAC instrument handbook as

$$\tilde{\beta} = \frac{(\sum I_i)^2}{\sum (I_i^2)} \tag{1}$$

in which I_i is the intensity in a given pixel *i*. The noise pixel parameter is equal to one over the sharpness parameter S_1, (Muller & Buffington 1974), and proportional to the full width at half-maximum of the stellar point-spread function squared (Mighell 2005); for a more thorough discussion of the noise pixel parameter, please see Appendix A of Lewis et al. (2013). We generate two additional aperture populations using the noise pixel parameter: $\sqrt{\tilde{\beta}} \times [0.6, 0.7, 0.8, 0.85, 0.9, 0.95, 1.0, 1.05, 1.1, 1.15, 1.2]$ and $\sqrt{\tilde{\beta}} + [-0.8, -0.7, -0.6, -0.5, -0.4, -0.3, -0.2, -0.1, 0, 0.1, 0.2, 0.3, 0.4]$. We find that a fixed aperture size of 2.7 pixels produces the smallest amount of scatter in the final residuals, which is also consistent with our conclusions for previous 4.5 μm phase curve observations (Knutson et al. 2012; Lewis et al. 2013).

Outliers in the measured flux, *x*- and *y*-positions of the target, or the noise pixel parameter $\tilde{\beta}$ are removed by first discarding 6σ outliers and then by using a moving median filter with a width of 10 points and discarding outliers greater than 4σ. After applying this filter, we found that there were two points in our

Table 1
Photometric Data

JD (BJD_UTC −	Raw, Filtered Photometry		Final, Corrected Photometry	
2455214)	Relative Flux	Uncertainty	Relative Flux	Uncertainty
0.413525	1.007950	0.008475	1.002779	0.003201
0.413530	1.009589	0.008482	1.004326	0.003201
0.413535	1.009016	0.008479	1.002103	0.003201
0.413539	1.003937	0.008458	0.997562	0.003201
0.413544	1.011562	0.008490	1.004216	0.003201
0.413548	1.006882	0.008470	0.998892	0.003201
0.413553	1.005686	0.008465	0.998323	0.003201
0.413557	1.009775	0.008482	1.002209	0.003201
0.413562	1.006700	0.008469	0.999762	0.003201
0.413566	1.003509	0.008456	0.996224	0.003201

Note. Sample of the filtered, raw data (see Figure 1) and the final, corrected photometry (see Figure 2).

(This table is available in its entirety in a machine-readable form in the online journal. A portion is shown here for guidance regarding its form and content.)

observations (at BJD_UTC ≈ 2455214.9 and ≈2455217.29) in which the star displayed a sudden, sharp excursion in position typically lasting several minutes. These excursions are most likely the result of micrometeorite hits and we exclude them from our subsequent analysis. The two excluded segments of the light curve contain a total of 984 images, corresponding to 0.13% of the total data set. This raw, filtered data is presented in Table 1.

2.2. Flux Ramp Correction

Previous *Spitzer*/IRAC observations (e.g., Beerer et al. 2011; Todorov et al. 2012; Knutson et al. 2012; Lewis et al. 2013) note a ramp-like change in the observed flux at 4.5 μm, lasting approximately one hour. Agol et al. (2010) examined a similar effect in the 8 μm bandpass and postulated that the effect might be due to a combination of thermal settling of the telescope and charge-trapping in the array. This effect is mitigated by trimming the first hour of data after the start of the observation and again after the downlink break (at phase ≈0.75). We then fit the trimmed data with the ramp function given by Agol et al. (2010), as part of our global fit described in Section 2.3:

$$F'/F = 1 + a_1 e^{-t/a_2} + a_3 e^{-t/a_4},\quad (2)$$

in which F' is the flux with the ramp, F is the flux corrected for the ramp, a_1–a_4 are the correction coefficients, and t is the time. A Bayesian Information Criterion (BIC[12]; Schwarz 1978) analysis indicates that a ramp correction is unnecessary in order to fit the trimmed data. We therefore leave this ramp function out of our subsequent analysis, consistent with our previous 4.5 μm phase curve analyses (Knutson et al. 2012; Lewis et al. 2013).

2.3. Spitzer/IRAC Decorrelation

Previous studies of transiting exoplanets find that the largest error source in *Spitzer*/IRAC 3.6 and 4.5 μm data is due to intra-pixel sensitivity variations, which cause variations in the telescope pointing to manifest as changes in the measured flux from the target star (e.g., Charbonneau et al. 2008; Beaulieu et al. 2010; Ballard et al. 2010; Knutson et al. 2012; Lewis et al. 2013). This effect can be easily seen in our 4.5 μm full-orbit data (Figure 1) in which the raw flux tracks with the *x*-
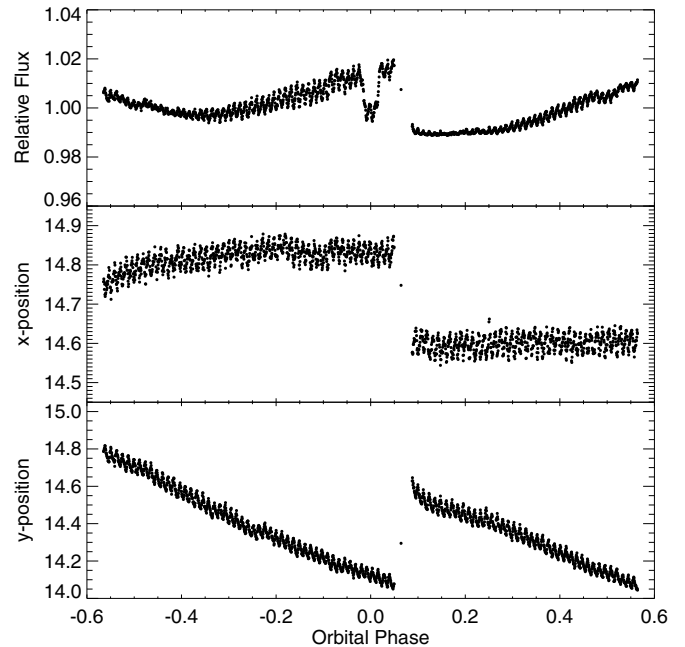

Figure 1. Raw *Spitzer*/IRAC2 4.5 μm full-orbit photometry of the exoplanet HD 209458b (top), its *x*-position (middle), and *y*-position on the array (bottom) vs. the orbital phase after filtering. All frames are binned by 400 data points (≈2.5 minutes). The gap in the data is due to spacecraft downlink. The raw flux is highly correlated with the *x*- and *y*-positions on the array, which we remove here with a pixel-mapping Gaussian detrending method (see Section 2.3).

and *y*-positions on the detector. We de-trend the data using a pixel-mapping Gaussian weight decorrelation method (Ballard et al. 2010; Knutson et al. 2012; Lewis et al. 2013) in which each photometric measurement is corrected by its 50 nearest neighbors in *x*-, *y*-, and $\tilde{\beta}$-space (see Equation (2) in Knutson et al. 2012). We find, consistent with Lewis et al. (2013), that inclusion of the noise pixel parameter $\tilde{\beta}$ terms increases the scatter in our final solutions. We therefore use the following simplified version of this correction instead:

$$F_{\text{meas},j} = F_{0,j} \sum_{i=0}^{n} e^{-(x_i - x_j)^2/2\sigma_{x,j}^2} \times e^{-(y_i - y_j)^2/2\sigma_{y,j}^2},\quad (3)$$

in which $F_{\text{meas},j}$ is the measured flux in the jth image; $F_{0,j}$ is the intrinsic flux; x_j and y_j are the measured *x*-position and *y*-position; and $\sigma_{x,j}$ and $\sigma_{y,j}$ are the standard deviations of the *x* and *y* vectors over the full range in *i* (0 to *n*, where $n = 50$ nearest neighbors). The 50 nearest neighbors to the jth image are determined via

$$d_{i,j} = \sqrt{(x_i - x_j)^2 + (y_i - y_j)^2},\quad (4)$$

in which $d_{i,j}$ is the distance vector between the jth image and the ith image; x_i and x_j are the measured *x*-positions of the ith and j^{th} images, respectively; and y_i and y_j are the measured *y*-positions of the ith and j^{th} images, respectively. As a first-order estimation, we set the uncertainties on individual flux values equal to the standard deviation of the normalized residuals (SDNR) of the raw flux divided by the Gaussian weight (see Equation (3)).

We employ a Levenburg–Marquardt least-squares minimization via the Interactive Data Language mpfit function (Markwardt 2009) to solve simultaneously for the best-fit transit, secondary eclipse, and phase curve functions while optimizing the corresponding pixel map at each step in our minimization.

Table 2
Global Fit Parameters

Parameter	Value	Uncertainty	
Orbital Parameters			
i (radians)	1.5131	−0.0017	+0.0016
a/R_s	8.810	−0.069	+0.064
Primary Transit Parameters			
T_c (BJD−2455000)	216.405640	−0.000097	+0.000091
R_p/R_s	0.12130	−0.00031	+0.00028
Secondary Eclipse Parameters			
First secondary eclipse depth	0.1243%	−0.0067%	+0.0073%
T_c (BJD−2455000)	214.6462	−0.0012	+0.0011
Second secondary eclipse depth	0.1391%	−0.0069%	+0.0072%
T_c (BJD−2455000)	218.1694	−0.0011	+0.0010
Average secondary eclipse depth	0.1317%	−0.0048%	+0.0051%
Phase Curve Parameters			
c_1	−0.0410%	−0.0046%	+0.0051%
c_2	0.0354%	−0.0063%	+0.0062%
Amplitude	0.109%	−0.011%	+0.012%
Minimum flux	1.000443	−0.000067	+0.000068
Minimum flux offset (hr)	−9.6	−1.4	+1.4
Minimum flux offset (°)	−40.9	−6.0	+6.0
Maximum flux	1.001527	−0.000036	+0.000036
Maximum flux offset (hr)	−9.6	−1.4	+1.4
Maximum flux offset (°)	−40.9	−6.0	+6.0

Table 3
Brightness Temperatures

Parameter	Temperature (K)
Secondary Eclipse Parameters	
First secondary eclipse	1380 ± 32
Second secondary eclipse	1443 ± 30
Average secondary eclipse	1412 ± 22
Phase Curve Parameters	
Amplitude	527 ± 46
Minimum flux	972 ± 44
Maximum flux	1499 ± 15

We first use a Mandel & Agol (2002) model light curve modified for full-orbit observations to calculate primary transit and secondary eclipse light curves using an initial guess for the system parameters, then divide those out of the raw light curve before making an initial pixel map. We next calculate a pixel map and corresponding correction (Equation (3)) for the intrapixel sensitivity variations at each point in the light curve. Thus, the Levenburg–Marquardt performs an iterative fit in which it finds the light curve model that, when the data is divided by the model, gives the best x- and y-position decorrelation (or pixel map) which minimizes the scatter in the corrected data/residuals.

For this analysis, the orbital period ($P = 3.5247455$ days) and eccentricity ($e = 0$) are fixed to values from a previous multi-transit study (Torres et al. 2008) while the stellar limb darkening coefficients ($ld_{1-4} = [0.4614, −0.4277, 0.3362, −0.1074]$) are derived from a three-dimensional (3D) model stellar atmosphere (Hayek et al. 2012). The inclination i, ratio of semi-major axis to stellar radius a/R_s, mid-transit time T_c, ratio of planetary to stellar radius R_p/R_s, secondary mid-eclipse times T_c, and secondary eclipse depths are left as free parameters. We also search for longitudinal brightness variations across the face of HD 209458b by fitting the full-orbit light curve with the Cowan & Agol (2008) phase curve function:

$$F = 1 + c_0 + c_1 \cos(2\pi t/P) + c_2 \sin(2\pi t/P)$$
$$+ c_3 \cos(4\pi t/P) + c_4 \sin(4\pi t/P), \quad (5)$$

in which c_0 is the secondary emission of the planet (here, we use the deeper measured secondary eclipse depth to establish this baseline so that it has a relative flux of unity), $c_1 − c_4$ are free parameters, t is the time, and P is the planetary orbital period. The BIC indicates that inclusion of this phase curve function is necessary and that the c_3 and c_4 terms do not improve the quality of the fit; therefore, only the c_1 and c_2 terms are used in the final fit. Fitting simultaneously for the phase curve, transit, and secondary eclipse models allows us to accurately account for the effect that the phase curve shape has on our estimates of the various transit and secondary eclipse parameters (Kipping & Tinetti 2010). After finding an initial full-orbit solution to

the data set, the photometric uncertainties are then inflated by a factor of 2.2 in order to produce a global best-fit solution with a reduced χ^2 equal to unity.

Next we explore the global solution-space with a Markov Chain Monte Carlo analysis (MCMC; e.g., Ford 2005). The initial best-fit parameter solutions are randomly perturbed to seed six independent MCMC chains each consisting of 10^5 links (steps). In each MCMC chain, a new trial solution is drawn from a Gaussian-distributed parameter space based upon the Levenburg–Marquardt best-fit parameters and associated uncertainties. Multiple (six) sufficiently long (10^5 links) MCMC chains are run with different randomly selected starting values to ensure both that an adequate amount of parameter space is sampled and that all chains converge to the global, and not a local, solution. After running each MCMC chain, we search for the point in which the chain has become well-mixed, as defined by where the χ^2 value first falls below the median of all the χ^2 values in the chain, and discard all links up to that "burn-in" point. A Gelman–Rubin test (Gelman & Rubin 1992) indicates a potential scale reduction factor ⩽1.07 for all parameters (Ford 2005), suggesting that all six MCMC chains have converged to the same global solution.

Because MCMCs assume that the noise in the data is Gaussian and uncorrelated from one measurement to the next, they will typically underestimate the true uncertainties for data with a significant component of time-correlated noise (Carter & Winn 2009). To account for this "red" correlated noise, we independently estimate the uncertainties on our fit parameters using the "residual permutation" or "prayer bead" method (e.g., Jenkins et al. 2002; Southworth 2008; Bean et al. 2008; Winn et al. 2008), in which the residuals from the best-fit MCMC solution are circularly permutated and added back onto the best-fit MCMC model to generate a new data set. A Levenburg–Marquardt fit is applied to each of these new "simulated" data sets in order to build up histograms of the best parameter distributions from each permutation. We then compare the resulting uncertainties to their counterparts from the MCMC analysis and take the larger of the two for each fit parameter as our final uncertainties. The prayer bead uncertainties were up to 2.6 times larger than the corresponding MCMC uncertainties. Our final fit parameters and their associated 1σ uncertainties are reported in Table 2 and the final, corrected photometry is presented in Table 1. The brightness temperatures calculated from the final fit parameters are listed in Table 3.

2.4. Residual Systematics

Despite the success of this reduction, some systematics still remain. For example, small oscillations in flux occur before and during the first secondary eclipse, and again near an orbital
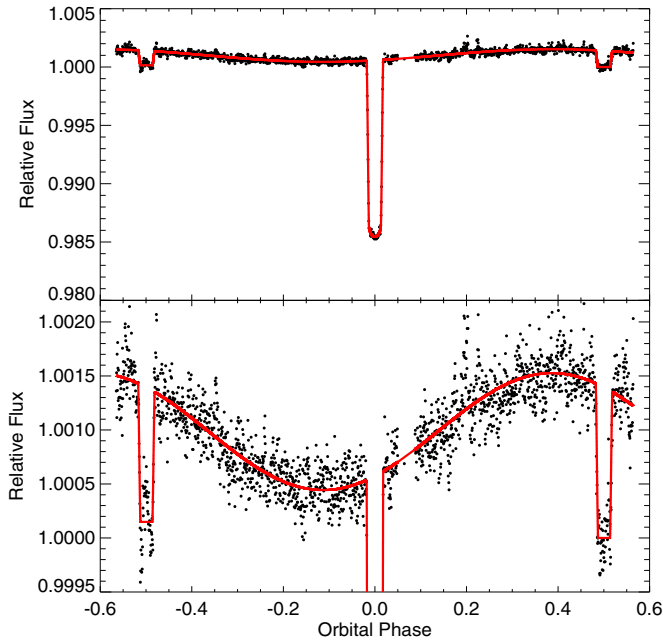
Figure 2. Final, decorrelated full-phase 4.5 μm light curve of HD 209458b. The "bumps" just prior to the first secondary eclipse, in the middle of the first secondary eclipse, and at a phase ≈0.2 are likely due to residual systematic errors or possibly stellar activity (see Section 2.4).

(A color version of this figure is available in the online journal.)

phase of 0.2. These features are not correlated with any change in x, y, or $\tilde{\beta}$, suggesting that they are not associated with any changes in *Spitzer's* pointing. In addition, they do not correspond with any background flux changes. These features could be due to stellar brightness variations from HD 209458, as their 0.1% amplitude is similar to the amplitude of flux variations measured for the Sun (Eddy 2009). However, the shape of the observed flux oscillations does not appear to match the sharp rise and slow decline expected for stellar flares (e.g., Figure 2 in Gary et al. 2012), and the timescale is too short for rotational spot modulations. Based on HD 209458's Ca II H and K emission measurements (log(R'_{HK}) = −4.97; Knutson et al. 2010), HD 209458 appears to have an activity level comparable
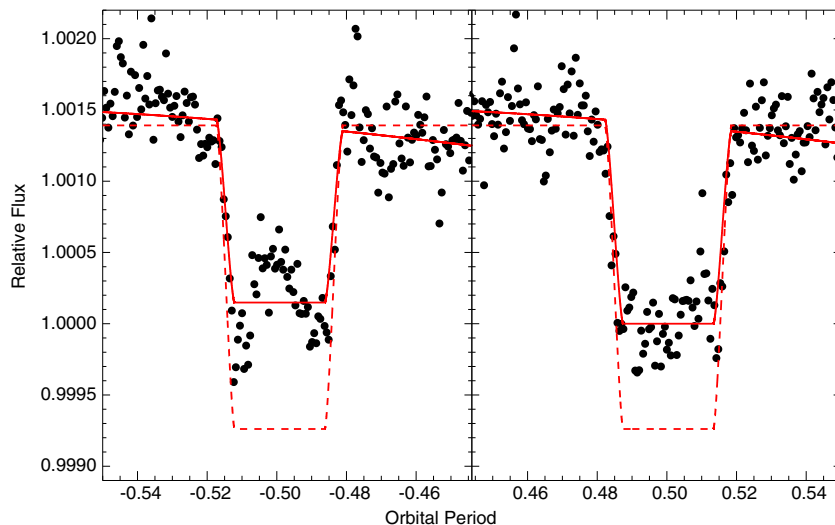

Figure 4. Standard deviation of the residuals vs. bin size for the final, decorrelated 4.5 μm full-orbit data. The red line is assuming pure Gaussian noise ($\propto 1/\sqrt{N}$, where N is the bin size). Bin sizes of 10^2 and 10^3 correspond to time intervals of ∼0.7 minutes and ∼7.5 minutes, respectively.

(A color version of this figure is available in the online journal.)

to that of our own Sun (log(R'_{HK}) = −4.96; Noyes et al. 1984); therefore, it might be reasonable to expect similar levels of infrared variability. Knutson et al. (2012) observed similar features in their *Spitzer*/IRAC HD 189733b data just after the first secondary eclipse at 3.6 μm and possibly before and after the second secondary eclipse at 4.5 μm. This similarity suggests that the features in our light curve might instead be the result of residual uncorrected *Spitzer*/IRAC systematics. We leave a full exploration of these features for a future study and note that they do not significantly affect the overall shape of the phase curve, the primary transit, or the second secondary eclipse.

3. RESULTS

The success of this reduction method is indicated by the decorrelated data (Figures 2 and 3) having a SDNR (the standard deviation of the normalized residuals) of 0.0032 which is within 14% (1.14 times) the photon noise limit. We estimate the significance of the red noise by calculating the rms of the residuals in bins of increasing size, as shown in Figure 4 and by

Figure 3. Comparison of our two final, decorrelated 4.5 μm secondary eclipses of HD 209458b and corresponding best-fit model (red line) with the best-fit model of Knutson et al. (2008; red dashed line). Here we find significantly (∼35%) shallower secondary eclipse values than Knutson et al. (2008).

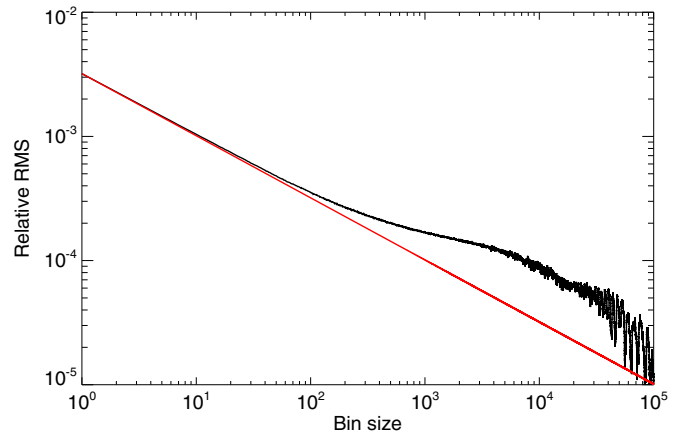(A color version of this figure is available in the online journal.)

using the Equation from Gillon et al. (2006):

$$\sigma_N^2 = \frac{\sigma_w^2}{N} + \sigma_r^2, \qquad (6)$$

where σ_N is the measured uncertainty for a bin size N, σ_w is the white noise and assumed to be equal to the SDNR, and σ_r is the red noise. Using Equation (6), we estimate the contribution of the red noise on relevant timescales. This value is 2.7% of the total scatter in the relative flux corresponding to a 2.7 increase in the total noise in the 1 hr bins, the timescales of eclipse ingress and egress. Our final global solutions and their 1σ uncertainties are listed in Table 2. The best-fit planet–star radius ratio is $R_p/R_s = 0.12130^{+0.00028}_{-0.00031}$, which is in good agreement with the previously published 4.5 μm measurement of 0.12174 ± 0.00056 (Beaulieu et al. 2010). We find a secondary eclipse depth ($0.1391\%^{+0.0072\%}_{-0.0069\%}$) that is inconsistent with the previously published value from Knutson et al. (2008) at the 4.4σ level (see Figures 3 and 5); we discuss possible reasons for this disagreement in Section 4.1.

4. DISCUSSION

4.1. Secondary Eclipse Emission

The revision of the previous 4.5 μm emission measurement by Knutson et al. (2008) is significant because the high brightness temperatures at 4.5 and 5.8 μm were interpreted as evidence for a thermal inversion (Burrows et al. 2007; Knutson et al. 2008; Madhusudhan & Seager 2009, 2010; Line et al. 2014). Our revision of HD 209458b's 4.5 μm emission is not without precedent. The original studies of both HD 189733b (Charbonneau et al. 2008) and HD 209458b (Knutson et al. 2008) were carried out by continuously cycling between the four IRAC arrays in order to cover all four bands during a single secondary eclipse. This method reduced the effective cadence of these observations to one-fifth that of the now standard staring mode observations, in which the star is observed continuously in a single band. The decision to cycle between detectors resulted in a significantly higher level of pointing jitter and correspondingly large flux variations in the resulting light curves as compared to staring mode observations. The disadvantages of this mode became apparent soon after these data were taken, and no other stars were observed in this manner. Although the original data were reduced using the standard techniques available at the time (namely, fitting with a polynomial function of x- and y-position), it would not be surprising if the large pointing jitter resulted in a biased estimate of the eclipse depth. Subsequent observations of HD 189733b by Knutson et al. (2012) used the now standard staring mode and pixel mapping techniques, and found a 3.6 μm eclipse depth that deviated by approximately 7.5σ from the previous value. It is therefore not surprising that our new staring mode observations of HD 209458b also result in a 4.4σ revision to the published eclipse depth.

Our revised estimate for the 4.5 μm brightness temperature agrees significantly better with published models for this planet (Figure 5). Despite the original interpretation of the Knutson et al. (2008) data as resulting from a thermal inversion, it is worth emphasizing that even one-dimensional radiative-equilibrium models with several tunable free parameters (Burrows et al. 2007; Fortney et al. 2008) had difficulty simultaneously explaining all four IRAC observations. Models in which the relative abundances and pressure-temperature profiles were allowed to vary as free parameters were able to match all four of the original measurements (Madhusudhan & Seager 2009, 2010; Line
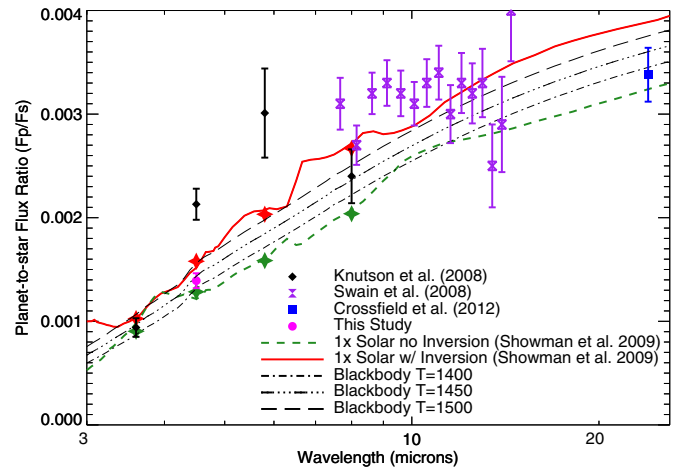

Figure 5. Comparison of the planet-to-star flux ratio (F_p/F_s) emission measurements of HD 209458b by Knutson et al. (2008; black diamonds), Swain et al. (2008; purple hourglasses), Crossfield et al. (2012; blue square), and this study (magenta circle; here, we plot the measurement from the second secondary eclipse $F_p/F_s = 0.1391\%^{+0.0072\%}_{-0.0069\%}$). Note how our revised 4.5 μm emission measurement brings this point into better agreement with the $1\times$ solar abundance models with and without a thermal inversion (red line and green dashed line, respectively; these models are also binned to the IRAC bandpasses as indicated by the star symbol) by Showman et al. (2009). Our new measurement also agrees reasonably well with blackbody emission curves with $T = 1400$ (dash dot line), $T = 1450$ (dash dot dot dot line), and $T = 1500$ (long dash line).

(A color version of this figure is available in the online journal.)

et al. 2014). These "data-driven" best-fit models find the temperature inversion placed where they have the most leverage over the 4.5 and 5.8 μm bandpasses. GCM simulations including a hot stratosphere generally do not produce elevated brightness temperatures at 4.5 and 5.8 μm relative to the other IRAC bandpasses Showman et al. (2009), since the pressures probed by the IRAC bandpasses largely overlap, and the depth of the inversion is not a free parameter, but is controlled by the optical and infrared opacity sources. As shown in Showman et al. (2009), in models where pressure–temperature profiles are not left as a free variable, much of the flux in the IRAC bandpasses is emitted to space from the bottom edge of, or even below, the inversion, implying that high stratospheric temperatures do not necessarily exert significant leverage on the flux emitted at 4.5 and 5.8 μm in these models. Furthermore, the inversion covers only part of the dayside in the 3D models, which also mutes its effect. However, there could be an absorber not accounted for in the models that gives rise to an inversion at a different level.

Our new analysis is in better agreement with the predictions of the general circulation models for this planet from Showman et al. (2009), including cases both with and without dayside temperature inversions, and also blackbody models (see Figure 5). Although our new measurement does not rule out a dayside temperature inversion, it suggests that an inversion may not be necessary to explain the current 4.5 μm broadband data. New high-precision eclipse measurements in the other *Spitzer* bandpasses, specifically photometry at 5.8 and 8 μm, and ideally mid-infrared spectroscopic measurements (e.g., Madhusudhan & Seager 2010; Burrows 2014; Line et al. 2014) would help to provide a more definitive answer to this question.

4.2. Phase Curve

Our derived 4.5 μm light curve indicates an eastward shifted hot spot, similar to the one observed for HD 189733b (Knutson et al. 2007, 2009b, 2012). Such eastward offsets were
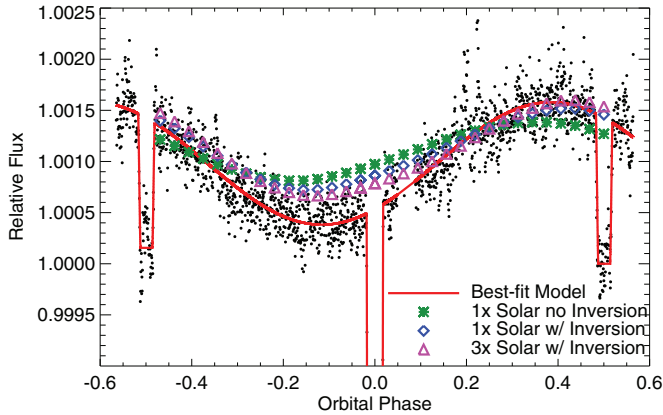
Figure 6. Comparison of our reduced data (black points) and its best-fit phase curve model (red line) to the Showman et al. (2009) GCMs with 1× solar abundance and no thermal inversion (green asterisks), an inversion with 1× solar abundance (blue diamonds), and an inversion with 3× solar abundance (magenta triangles). The Showman et al. (2009) inversion model predictions (blue diamonds and magenta triangles) nominally fit our observations, except on the nightside in which the GCM overpredicts HD 209458b's flux.

(A color version of this figure is available in the online journal.)

first predicted for hot Jupiters by Showman & Guillot (2002), and subsequent 3D circulation models confirm that they are a robust feature of the hot-Jupiter circulation regime, at least over a certain range of incident stellar fluxes and atmospheric radiative time constants (e.g., Cooper & Showman 2005; Showman et al. 2008a, 2009, 2013; Menou & Rauscher 2009; Rauscher & Menou 2010, 2012; Heng et al. 2011b, 2011a; Perna et al. 2012; Dobbs-Dixon et al. 2012). In these circulation models, the eastward offset of the hot spot results from advection of the temperature field by a fast, broad eastward equatorial jet stream—so-called equatorial superrotation. In turn, the equatorial superrotation results from interactions with the mean flow of standing, planetary-scale waves induced by the day-night heating contrast (Showman & Polvani 2011). When the radiative time constant is comparable to the characteristic timescale for air parcels to advect eastward over a planetary radius, then significant eastward hot spot offset from the substellar point should occur. Overall, our observations are consistent with this body of theory and models, and suggest that HD 209458b likely exhibits equatorial superrotation at photospheric levels.

Figure 6 compares our best-fit model of HD 209458b's observed full-orbit flux to theoretical phase curves generated from the GCMs presented in Showman et al. (2009). The Showman et al. (2009) 3D dynamical models of HD 209458b are the first with non-gray radiative transfer across the entire wavelength range from the visible through the infrared. In our observations, we find a phase curve maximum that occurs 9.6 ± 1.4 hr before secondary eclipse, corresponding to a hot spot shifted $40^{\circ}.9 \pm 6^{\circ}.0$ eastward of the substellar point. The theoretical phase curves generated from the GCM are shown for no-thermal-inversion models (i.e., models lacking TiO and VO), and models with TiO and VO included at 1× and 3× solar abundance. These molecules cause a thermal inversion due to the extreme opacity of TiO and VO in the visible.[13] Interestingly, our observations exhibit a peak flux in the light curve which leads secondary eclipse by an amount intermediate to that predicted from the no-inversion and thermal-inversion

models. Overall, our observed dayside emission (phase ∼0.25 to 0.75 in Figure 6) matches the predictions of the Showman et al. (2009) models well, especially for models including visible absorbers and a dayside inversion.

There exist a variety of factors that can influence the offsets of the hot spot for a given hot Jupiter. Generally speaking, a larger atmospheric opacity would move the photospheres to higher altitude (lower pressure), in which the radiative time constant is shorter, leading to a smaller hot-spot offset; and conversely for smaller atmospheric opacity (Dobbs-Dixon & Lin 2008; Showman et al. 2009; Lewis et al. 2010; Heng et al. 2011a). Such opacity variations could result from the gas metallicity (higher metallicity generally implies greater opacity and vice versa), or potentially from hazes, though there is currently no strong evidence that hazes significantly affect the emission on HD 209458b (Deming et al. 2013). Moreover, for specified opacities, the existence of atmospheric frictional drag could lead to slower wind speeds, decreasing the hot spot offset, potentially even to zero if the drag is sufficiently strong (Rauscher & Menou 2012; Showman et al. 2013; Dobbs-Dixon et al. 2012). Such drag could result from Lorentz forces due to the partial thermal ionization at high temperatures (Perna et al. 2010; Rauscher & Menou 2013; Rogers & Showman 2014). Nevertheless, the fact that our observed offset is significantly nonzero (with 6.9σ confidence) and agrees reasonably well with GCM simulations performed in the absence of strong drag at photospheric levels (Figure 6; Showman et al. 2009) suggests that these magnetohydrodynamic effects do not play a dominant role in controlling the hot spot offset for HD 209458b.

HD 209458b's observed phase curve, which represent the first $4.5\,\mu\mathrm{m}$ measurements of its nightside emission, indicates that HD 209458b has a day-to-night temperature contrast of $\Delta T_{obs} = 527 \pm 46$ K. We find that HD 209458b has a smaller contrast at $4.5\,\mu\mathrm{m}$ ($A_{obs} = 0.352 \pm 0.031$[14]) than other hot Jupiters with higher levels of incident flux (e.g., WASP-12b and WASP-18b; Cowan et al. 2012; Maxted et al. 2013, respectively), consistent with the idea that this temperature contrast is driven by insolation (Perez-Becker & Showman 2013) as the radiative time constant decreases with increasing temperature (Showman & Guillot 2002). However, the only day-night temperature contrast measurements that exist for HD 209458b are at $4.5\,\mu\mathrm{m}$ (presented here) and an upper-limit at $8\,\mu\mathrm{m}$ (Cowan et al. 2007). Thus full-orbit phase curve measurements both at additional wavelengths, such as $3.6\,\mu$m, and for other targets are necessary to confirm the hypothesis of Perez-Becker & Showman (2013).

In addition, HD 209458b's phase curve suggests that the nightside is much cooler than predicted by Showman et al. (2009). Yet, while the location of the 1× and 3× solar abundance inversion phase curve minima (Showman et al. 2009) more closely agree with our observations compared to the no inversion model, the GCM overestimates the nightside flux, thereby underestimating the total day-to-night temperature contrast ($\Delta T_{GCM} \approx 300$ K versus $\Delta T_{obs} = 527 \pm 46$ K). The Showman et al. (2009) models similarly overpredict HD 189733b's nightside emission compared to *Spitzer*/IRAC full phase observations by Knutson et al. (2012). This discrepancy is attributed to disequilibrium carbon chemistry not included in the GCM, in particular quenching, which would increase the abundances of CO and CH_4 at higher altitudes so that measurements would be probing a comparably higher optically thick layer with cooler temperatures. In the

---

[13] TiO and VO are simply proxies for any visible-wavelength absorber in these models, and any other strong visible absorber would lead to qualitatively similar behavior.

---

[14] $A_{obs} = (\mathrm{flux_{day}} - \mathrm{flux_{night}})/\mathrm{flux_{day}}$ (Perez-Becker & Showman 2013).

HD 209458b abundance profiles of Showman et al. (2009) and Moses et al. (2011), the vertical CO abundance profile is driven by chemical equilibrium, resulting in a relatively constant mixing ratio from 10 to 10^{-8} bars. Therefore vertical quenching of CO would have a minimal effect on its abundance profile, suggesting that vertical quenching of CO is likely not the culprit for HD 209458b's cooler observed nightside. However, the Moses et al. (2011) abundance profiles of CH_4 suggest that vertical quenching can increase the CH_4 abundance by nearly an order of magnitude from 1 to 10^{-5} bars compared to the equilibrium-driven Showman et al. (2009) profiles. This additional CH_4 could potentially help radiate heat and result in an overall cooler nightside than predicted by the GCM. To determine if quenched CH_4 is causing the nightside cooling, we are in the process of measuring HD 209458b's full-orbit phase curve at 3.6 μm, which overlaps the CH_4 ν_3 band. Analyses of these data with future GCM studies, which include both non-equilibrium chemistry and new hot CH_4 line lists (Yurchenko & Tennyson 2014), will better constrain the properties of these two carbon-bearing species and the nightside cooling mechanism.

5. CONCLUSIONS

Here we present the first measurements of HD 209458b's 4.5 μm full-orbit phase curve using *Spitzer*/IRAC. Our data indicate 0.69σ agreement with a previous primary transit depth by Beaulieu et al. (2010) and revise HD 209458b's secondary eclipse emission measurement by Knutson et al. (2010) downward by $\sim$35%, potentially weakening the evidence for a dayside temperature inversion. The phase-curve observations suggest both a hot spot shifted eastward of the substellar point and a day-to-night temperature contrast smaller than that of more highly irradiated hot Jupiters, suggesting that this contrast may be driven by the incident stellar flux. The shape of the phase curve, specifically the location and brightness temperature of the hot spot, suggests that HD 209458b could have a dayside inversion at a pressure level that is between that predicted by non-inversion models and that predicted by TiO and VO induced thermal inversion models ($\gtrsim$0.008 bar) (Showman et al. 2009). However, new GCMs that include non-equilibrium chemistry and hot CH_4 lines (Yurchenko & Tennyson 2014) are necessary not only to confirm this hypothesis but also determine why HD 209458b's nightside is cooler than previously predicted. Thus, while we cannot draw any strong conclusions on HD 209458b's thermal inversion, we hope to better constrain the existence of a thermal inversion with upcoming full-orbit phase curve observations at 3.6 μm and eclipse mapping at both 3.6 and 4.5 μm.

REFERENCES

Agol, E., Cowan, N. B., Knutson, H. A., et al. 2010, ApJ, 721, 1861
Ballard, S., Charbonneau, D., Deming, D., et al. 2010, PASP, 122, 1341
Bean, J. L., Benedict, G. F., Charbonneau, D., et al. 2008, A&A, 486, 1039
Beaulieu, J. P., Kipping, D. M., Batista, V., et al. 2010, MNRAS, 409, 963
Beerer, I. M., Knutson, H. A., Burrows, A., et al. 2011, ApJ, 727, 23
Borucki, W. J., Koch, D., Jenkins, J., et al. 2009, Sci, 325, 709
Burrows, A., Hubeny, I., Budaj, J., Knutson, H. A., & Charbonneau, D. 2007, ApJL, 668, L171
Burrows, A. S. 2014, PNAS, in press
Carter, J. A., & Winn, J. N. 2009, ApJ, 704, 51
Charbonneau, D., Brown, T. M., Latham, D. W., & Mayor, M. 2000, ApJL, 529, L45
Charbonneau, D., Knutson, H. A., Barman, T., et al. 2008, ApJ, 686, 1341
Cooper, C. S., & Showman, A. P. 2005, ApJL, 629, L45
Cooper, C. S., & Showman, A. P. 2006, ApJ, 649, 1048
Cowan, N. B., & Agol, E. 2008, ApJL, 678, L129
Cowan, N. B., Agol, E., & Charbonneau, D. 2007, MNRAS, 379, 641
Cowan, N. B., Machalek, P., Croll, B., et al. 2012, ApJ, 747, 82
Crossfield, I. J. M., Knutson, H., Fortney, J., et al. 2012, ApJ, 752, 81
Deming, D., Seager, S., Richardson, L. J., & Harrington, J. 2005, Natur, 434, 740
Deming, D., Wilkins, A., McCullough, P., et al. 2013, ApJ, 774, 95
Désert, J.-M., Vidal-Madjar, A., Lecavelier Des Etangs, A., et al. 2008, A&A, 492, 585
Dobbs-Dixon, I., Agol, E., & Burrows, A. 2012, ApJ, 751, 87
Dobbs-Dixon, I., & Lin, D. N. C. 2008, ApJ, 673, 513
Eddy, J. A. 2009, The Sun, the Earth and Near-Earth Space: A Guide to the Sun-Earth System (Washington, DC: NASA)
Fazio, G. G., Hora, J. L., Allen, L. E., et al. 2004, ApJS, 154, 10
Ford, E. B. 2005, AJ, 129, 1706
Fortney, J. J., Lodders, K., Marley, M. S., & Freedman, R. S. 2008, ApJ, 678, 1419
Gary, B. L., Hebb, L. H., Foote, J. L., et al. 2012, SASS, 31, 17
Gelman, A., & Rubin, D. B. 1992, StaSc, 7, 457
Gillon, M., Pont, F., Moutou, C., et al. 2006, A&A, 459, 249
Harrington, J., Hansen, B. M., Luszcz, S. H., et al. 2006, Sci, 314, 623
Hayek, W., Sing, D., Pont, F., & Asplund, M. 2012, A&A, 539, A102
Heng, K., Frierson, D. M. W., & Phillipps, P. J. 2011a, MNRAS, 418, 2669
Heng, K., Menou, K., & Phillipps, P. J. 2011b, MNRAS, 413, 2380
Henry, G. W., Marcy, G. W., Butler, R. P., & Vogt, S. S. 2000, ApJL, 529, L41
Jenkins, J. M., Caldwell, D. A., & Borucki, W. J. 2002, ApJ, 564, 495
Kipping, D. M. 2008, MNRAS, 389, 1383
Kipping, D. M., & Tinetti, G. 2010, MNRAS, 407, 2589
Knutson, H. A., Charbonneau, D., Allen, L. E., Burrows, A., & Megeath, S. T. 2008, ApJ, 673, 526
Knutson, H. A., Charbonneau, D., Allen, L. E., et al. 2007, Natur, 447, 183
Knutson, H. A., Charbonneau, D., Cowan, N. B., et al. 2009a, ApJ, 703, 769
Knutson, H. A., Charbonneau, D., Cowan, N. B., et al. 2009b, ApJ, 690, 822
Knutson, H. A., Howard, A. W., & Isaacson, H. 2010, ApJ, 720, 1569
Knutson, H. A., Lewis, N., Fortney, J. J., et al. 2012, ApJ, 754, 22
Langton, J., & Laughlin, G. 2007, ApJL, 657, L113
Langton, J., & Laughlin, G. 2008, ApJ, 674, 1106
Laughlin, G., Marcy, G. W., Vogt, S. S., Fischer, D. A., & Butler, R. P. 2005, ApJL, 629, L121
Lewis, N. K., Knutson, H. A., Showman, A. P., et al. 2013, ApJ, 766, 95
Lewis, N. K., Showman, A. P., Fortney, J. J., et al. 2010, ApJ, 720, 344
Line, M. R., Knutson, H., Wolf, A. S., & Yung, Y. L. 2014, ApJ, 783, 70
MacDonald, G. J. F. 1964, RvGSP, 2, 467
Madhusudhan, N., & Seager, S. 2009, ApJ, 707, 24
Madhusudhan, N., & Seager, S. 2010, ApJ, 725, 261
Mandel, K., & Agol, E. 2002, ApJL, 580, L171
Markwardt, C. B. 2009, in ASP Conf. Ser. 411, Astron. Data Analysis Software and Syst. XVIII, ed. D. A. Bohlender, D. Durand, & P. Dowler (San Francisco, CA: ASP), 251
Maxted, P. F. L., Anderson, D. R., Doyle, A. P., et al. 2013, MNRAS, 428, 2645
Mazeh, T., Naef, D., Torres, G., et al. 2000, ApJL, 532, L55
Menou, K., & Rauscher, E. 2009, ApJ, 700, 887
Mighell, K. J. 2005, MNRAS, 361, 861
Moses, J. I., Visscher, C., Fortney, J. J., et al. 2011, ApJ, 737, 15
Muller, R. A., & Buffington, A. 1974, JOSA, 64, 1200
Noyes, R. W., Hartmann, L. W., Baliunas, S. L., Duncan, D. K., & Vaughan, A. H. 1984, ApJ, 279, 763
Parmentier, V., Showman, A. P., & Lian, Y. 2013, A&A, 558, A91
Peale, S. J. 1974, AJ, 79, 722

Perez-Becker, D., & Showman, A. P. 2013, ApJ, 776, 134
Perna, R., Heng, K., & Pont, F. 2012, ApJ, 751, 59
Perna, R., Menou, K., & Rauscher, E. 2010, ApJ, 719, 1421
Rauscher, E., & Menou, K. 2010, ApJ, 714, 1334
Rauscher, E., & Menou, K. 2012, ApJ, 750, 96
Rauscher, E., & Menou, K. 2013, ApJ, 764, 103
Richardson, L. J., Deming, D., Horning, K., Seager, S., & Harrington, J.
    2007, Natur, 445, 892
Richardson, L. J., Deming, D., & Seager, S. 2003, ApJ, 597, 581
Rogers, T. M., & Showman, A. P. 2014, ApJL, 782, L4
Rowe, J. F., Matthews, J. M., Seager, S., et al. 2008, ApJ, 689, 1345
Schwarz, E. 1978, AnSta, 6, 461
Showman, A. P. 2008, Natur, 452, 296
Showman, A. P., Cooper, C. S., Fortney, J. J., & Marley, M. S. 2008a, ApJ,
    682, 559
Showman, A. P., Cooper, C. S., Fortney, J. J., & Marley, M. S. 2008b, ApJ,
    682, 559

Showman, A. P., Fortney, J. J., Lewis, N. K., & Shabram, M. 2013, ApJ,
    762, 24
Showman, A. P., Fortney, J. J., Lian, Y., et al. 2009, ApJ, 699, 564
Showman, A. P., & Guillot, T. 2002, A&A, 385, 166
Showman, A. P., & Polvani, L. M. 2011, ApJ, 738, 71
Southworth, J. 2008, MNRAS, 386, 1644
Spiegel, D. S., Silverio, K., & Burrows, A. 2009, ApJ, 699, 1487
Swain, M. R., Bouwman, J., Akeson, R. L., Lawler, S., & Beichman, C. A.
    2008, ApJ, 674, 482
Swain, M. R., Tinetti, G., Vasisht, G., et al. 2009, ApJ, 704, 1616
Todorov, K. O., Deming, D., Knutson, H. A., et al. 2012, ApJ, 746, 111
Torres, G., Winn, J. N., & Holman, M. J. 2008, ApJ, 677, 1324
Werner, M. W., Roellig, T. L., Low, F. J., et al. 2004, ApJS, 154, 1
Winn, J. N., Holman, M. J., Torres, G., et al. 2008, ApJ, 683, 1076
Winn, J. N., Noyes, R. W., Holman, M. J., et al. 2005, ApJ, 631, 1215
Wittenmyer, R. A., Welsh, W. F., Orosz, J. A., et al. 2005, ApJ, 632, 1157
Yurchenko, S. N., & Tennyson, J. 2014, MNRAS, 440, 1649